Contents lists available at ScienceDirect

Superlattices and Microstructures

Review

Structural and optical properties of ZnO nanoparticles prepared by direct precipitation method

CrossMark

M. Kahouli [a,*], A. Barhoumi [a], Anis Bouzid [a], A. Al-Hajry [b], S. Guermazi [a]

[a] University of Sfax, Research Unit: PMISI, Faculty of Science Sfax, Route de la Soukra, km 3.5, B.P. n 1171, 3000 Sfax, Tunisia
[b] Promising Centre for Sensors and Electronic Devices (PCSED), Najran University, P.O. Box 1988, Najran 11001, Saudi Arabia

ARTICLE INFO

ABSTRACT

ZnO nanoparticles were synthesized by direct precipitation method at ambient conditions. Structural, thermal, morphological and optical properties of ZnO nanoparticles were investigated by X-ray diffraction (XRD), differential scanning calorimetry (DSC), scanning electron microscopy (SEM), energy dispersive spectroscopy (EDS), Ultraviolet–Visible spectroscopy and Raman spectroscopy. The XRD measurement shows that ZnO powder has a wurtzite structure. The grain size was estimated from Scherer's method and Williamson–Hall (W–H) plots. From DSC curve we can deduce the various endothermic and exothermic peaks obtained when the sample was heated from room temperature to 413 °C. The morphology and grain distribution of ZnO nanoparticles were analyzed by SEM. Optical properties were investigated by UV–Visible spectroscopy. The Tauc model was used to determine the optical gap energy of the synthesized ZnO particles. The observed Raman peak at 438 cm^{-1} was attributed to the E_2 (high) mode. The broad band at 569 cm^{-1} is due to disorder-activated Raman scattering for A_1 mode. These bands are associated with the first-order Raman active modes of the ZnO phase.

© 2015 Elsevier Ltd. All rights reserved.

---

* Corresponding author. Tel.: +216 42 46 08 68.
  E-mail address: Kahouli.majdi@yahoo.fr (M. Kahouli).

Contents

1. Introduction

Nowadays, there is an increasing demand for the development of nanosized semiconductors due to their significant electrical and optical properties which are highly useful for the fabrication of multifunctional nanoscaled optoelectronic and electronic devices. Among various semiconducting materials, wurtzite zinc oxide (ZnO) is a distinctive native n-type semiconductor with a wide and direct band gap (3.37 eV) and a high exciton binding energy (60 meV) at room temperature and excellent chemical stability [1,2]. It has a hexagonal structure with lattice parameters of $a = b = 3.250$ Å and $c = 5.206$ Å [3,4]. For this reasons, ZnO is used in several applications such as ultraviolet (UV) light emitters, piezoelectric devices, chemical and gas sensors, transistors, solar cells, catalysts and spintronics [5–8]. To obtain high quality ZnO nanopowders, a variety of techniques have been used such as, sol–gel, microemulsion, thermal decomposition of organic precursors, spray pyrolysis, electro-deposition, ultrasonic, microwave-assisted techniques, chemical vapor deposition and hydrothermal and precipitation methods [9–18]. Most of these techniques were not extensively used on a large scale. Direct precipitation synthesis has been widely used due to its simplicity and low cost. This paper deals with the synthesis of ZnO nanoparticles by direct precipitation method and discusses their structural, morphological, thermal and optical properties.

2. Experimental details

2.1. Powder synthesis

Direct precipitation method was employed to synthesize ZnO nanoparticles, which is based on chemical reactions between raw materials. The material was prepared from $ZnSO_4 \cdot 7H_2O$ (0.196 g), $HOOC(CH_2)_4COOH$ (0.100 g), NaOH (0.273 g) and distilled water (5 ml) in the molar ratio $ZnSO_4 \cdot 7H_2O:HOOC(CH_2)_4COOH = 1$. Once introduced in the above-mentioned order, reactants were stirred for few minutes. The precipitates were formed, and then filtered and washed with distilled water and acetone to remove the residues of $HOOC(CH_2)_4COOH$. The obtained powders were dried at ambient conditions for several hours.

2.2. Characterization techniques

Crystal structure of ZnO powder was investigated by using X-ray diffraction (XRD) having Cu K_{α} radiation (λ = 1.541 Å). Differential scanning calorimeter (DSC) was used to determine the thermal properties of ZnO powder. Morphology of the sample was investigated using scanning electron microscope (JEOL JSM-7600F) equipped with Oxford X-Max EDS detector for the compositional analysis of the synthesized ZnO nanoparticles. The optical absorption spectrum of ZnO was recorded using a UV–VIS spectrophotometer (lambda 950 PerkinElmer) in the wavelength range of 200–800 nm. Optical parameters such as the optical band gap E_g, absorption coefficient α, extinction coefficient k, refractive index n, dispersion parameter, dielectric constants and optical conductivity have been investigated. The dispersion energy, single-oscillator strength and refractive index at infinite wavelength of ZnO were estimated. Raman spectroscopy (RS) was performed to investigate the vibrational properties of the ZnO nanostructures at room temperature.

3. Results and discussion

3.1. Structural properties

X-ray diffraction pattern of ZnO powder is shown in Fig. 1. The presence of different peaks such as (100), (002), (101), (102), (110), (103), (200), and (112) confirm the hexagonal wurtzite structure of ZnO powder [19,20]. No other peaks related to impurities are observed, which proves the high purity of the wurtzite phase.

From XRD pattern, the interplanar spacing d_{hkl} values of ZnO powder were calculated using the Bragg equation Eq. (1) [21].

The lattice parameters a and c for the hexagonal structure are calculated using the relation given by Eq. (2) [22].

The lattice parameters c and a are determined from the (002) and (100) peaks using Eqs. (3) and (4).

The values of the lattice parameters c and a are found to be 5.211 Å and 3.250 Å, respectively (see Table 1).

The volume (V) of the unit cell for hexagonal system is calculated by using Eq. (5).

The lattice parameters c and a, and the volume V of ZnO nanoparticles synthesized in this work are comparable with those obtained in the JCPDS file No. 36-1451.
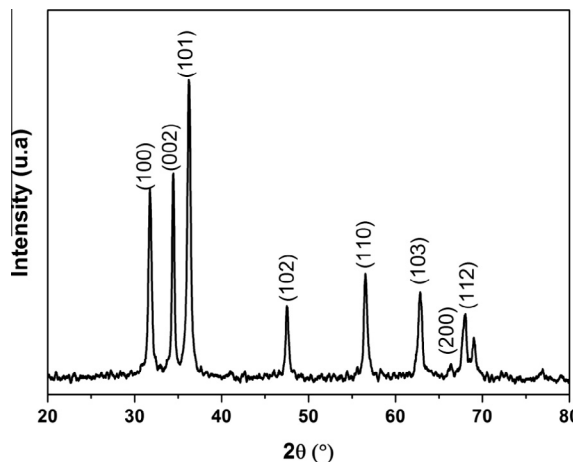

Fig. 1. XRD pattern of the ZnO powder.

Table 1
Lattice parameters (*c* and *a*), cell volume, and *c/a* ratio of ZnO nanoparticle.

	a (Å)	*c* (Å)	*c/a* ratio	Unit cell volume (Å^3)
Our sample	3.250	5.211	1.603	47.65
JCPDS 36-1451	3.249	5.206	1.602	47.63

Table 2
The texture coefficient and the percentage by volume of oriented crystallites.

JCPDS (36-1451)			Our sample				
h k l	2θ	*I*	2θ	*I*	Texture coefficient (TC)	Percentage of oriented crystallites χ (%)	Stacking fault probability α
(1 0 0)	31.76	57	31.82	58	0.902	8.2	0.053
(0 0 2)	34.42	44	34.48	63	1.265	11.4	0.048
(1 0 1)	36.25	100	36.23	90	0.796	8.1	0.015
(1 0 2)	47.53	23	47.48	25	0.964	9.81	0.028
(1 1 0)	56.60	32	56.66	34	0.938	9.54	0.028
(1 0 3)	62.86	29	62.78	29	0.884	9	0.033
(1 1 2)	67.96	23	67.85	22	0.846	8.64	0.041
(2 0 1)	69.09	11	68.04	16	0.601	6.3	0.393

In order to evaluate the texture coefficient and the percentage by volume crystallites oriented according to preferential directions, we used the formula Eq. (6) [23].

The values of TC (*h k l*) and the percentage of oriented crystallites χ (%) are shown in Table 2.

As shown in Table 2, the highest value of the texture coefficient TC$_{hkl}$ (1.265) and the percentage of oriented crystallites (11.4%) were observed for (0 0 2) peak. This proves that the crystallites have a preferential orientation according to (0 0 2) direction.

The lattice parameters *a* and *c* for ZnO nanoparticles synthesized in this work are 3.25 Å and 5.211 Å, respectively. As shown, the lattice parameter *c* is higher than c_0 which is the lattice parameter of ZnO powder without stress (5.206 Å) [24]. This shows that ZnO nanoparticles undergo a tensile stress in the direction of *c*-axis. Stresses are generated by a number of factors such as lattice strain due to the defects which will be confirmed by DSC measurements, inter-planar spacing, crystallite sizes, temperature gradients, structural changes, inelastic deformation [25] and the stacking faults. In the present work, the generation of residual stress has been discussed in relation to lattice strain, stacking fault and crystallite sizes, in particular. The stacking fault is a planar imperfection that arises from the stacking of one atomic plane out of sequence with another while the lattice on either side of the fault is perfect. The presence of a stacking fault gives rise to a shift in the peak positions observed relative to the ideal JCPDS (36-1451) of ZnO. From XRD patterns, the peak shift $\Delta(2\theta)$ for the oriented (*h k l*) planes was measured. The stacking fault probability α was calculated using Eq. (7) [26].

The obtained values were added in Table 2.

The residual stress σ can be estimated using the following equations Eq. (8) [27].

The value of the residual stress for ZnO nanoparticles is −0.217. The negative sign of σ shows that ZnO powders undergo a compressive stress perpendicular to the direction of *c*-axis.

The grain size *D* of ZnO powder was calculated from XRD patterns by using two methods.

3.1.1. Scherrer method

Firstly, according to Scherrer's equation [29], the grain size *D* could be calculated using β and θ, which are respectively, the FWHM and the Bragg's angle of different peaks using Eq. (9).

The grain size value calculated for the different XRD peaks of ZnO nanopowder is given in Table 3. The average grain size is 23.22 nm.

The dislocation density δ of ZnO powder was calculated from Eq. (10) [30].

Table 3
Structure parameters of ZnO nanopowders and average crystallite size estimated from averaging directly, slope of linear fit and dislocation density δ.

Peak	2θ (°)	FWHM (°)	D (nm)	δ (10^{-4} nm^{-2})	Average crystallite (nm) obtained by		
					Averaging	Linear fit	Linear fit through zero
(100)	31.825	0.377	22.182	20.323			
(002)	**34.486**	**0.237**	**35.410**	**7.975**	**23.22**	**31.07**	**21.29**
(101)	36.226	0.410	20.547	23.685			
(102)	47.4898	0.3292	26.575	14.159			
(110)	56.6608	0.4432	20.457	23.894			
(103)	62.7836	0.4103	22.87	19.106			
(200)	67.8576	0.3719	26.110	14.667			
(112)	68.0473	0.3719	26.139	14.635			

Values of δ for different XRD peaks are given in Table 3. The average dislocation density is found to be 17.617×10^{-4} nm^{-2}.

On the other hand, the grain size D can be estimated by using other methods like Williamson–Hall method. The significance of the broadening of peaks evidences grain refinement along with the large strain associated with the powder. The instrumental broadening (β_{hkl}) was corrected, corresponding to each diffraction peak of ZnO nanopowder using Eq. (11).

Using Eq. (9) we obtained Eq. (12).

A plot is drawn with $\frac{1}{\beta_{hkl}}$ on the x-axis and $\cos\theta$ on the y-axis for ZnO nanopowder as shown in Fig. 2. In order to calculate the average crystallite size, two approaches were used including averaging directly through crystallite sizes obtained for all peaks, estimating from the slope of the linear fit [31], as seen in Fig. 2. The results obtained from the Scherrer method are summarized in Table 3.

3.1.2. Williamson–Hall method

XRD peaks are broadened by small crystallite size and lattice distortion caused by lattice dislocations. However, the effect of strain and imperfections on the line broadening differs from the effect of crystalline size. The strain induced in ZnO nanopowders was calculated using Eq. (13) [31].

From Eqs. (9) and (13), it was confirmed that the peak width from crystallite size varies as $\frac{1}{\cos\theta}$ and from strain varies as $\tan\theta$. Assuming that the particle size and strain contributions to line broadening are independent to each other and both have a Cauchy-like profile, the observed line breadth is simply the sum of Eqs. (9), (13) and (14).
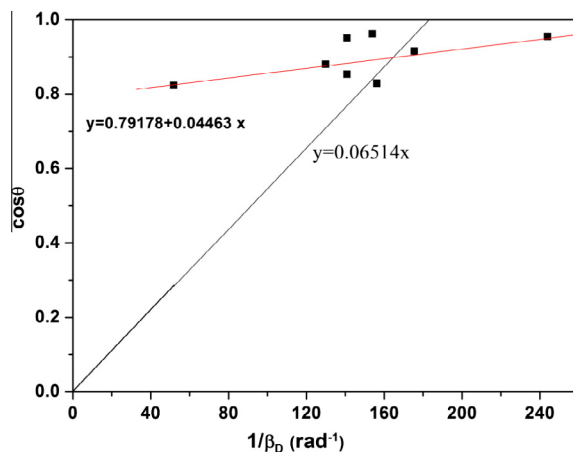

**Fig. 2.** Plot of $\cos\theta$ vs $1/\beta_{hkl}$ of ZnO sample.

By rearranging the above equation, we get Eq. (15).

To make a Williamson–Hall analysis, the term $\beta_{hkl}\cos\theta$ was plotted vs $4\sin\theta$ for all orientation peaks of ZnO with the wurtzite hexagonal phase with 2θ varies from 20° to 80°, as seen in Fig. 3. By fitting a straight line to the data, the crystallite size and strain are determined from the slope and y-intercept of the fit, respectively. Eq. (14) is written for the isotropic nature of crystal and represents UDM, where the strain in the material is assumed to be uniform in all crystallographic directions. The results obtained from UDM analysis for ZnO nanopowders are shown in Fig. 3 and gathered in Table 4. Uniform deformation stress and uniform deformation energy density were taken into account; the anisotropic nature of Young's modulus of the crystal is more realistic [32–34]. The generalized Hook's law referred to the strain, keeping only the linear proportionality between the stress and strain, i.e. $\sigma = \varepsilon E$. Here, the stress is proportional to the strain, with the constant of proportionality being the modulus of elasticity or Young's modulus, denoted by E. In this approach, the Williamson–Hall equation is modified by substituting the value of ε in Eq. (15), we get the following equation Eq. (16).

E_{hkl} is Young's modulus in the direction perpendicular to the set of the crystal lattice plane $(h\,k\,l)$. The uniform stress can be calculated from the slope line plotted between $4\sin\theta/E_{hkl}$ and $\beta_{hkl}\cos\theta$, and the crystallite size D from the intercept as shown in Fig. 4. With the knowledge of the values of E_{hkl} for the hexagonal ZnO, we determine the values of strain. For samples with a hexagonal crystal phase, Young's modulus E_{hkl} is related to their elastic compliances S_{ij} as given in Eq. (17) [35,36].

Young's modulus was calculated as ~130 MPa. Eq. (16) represents the UDSM. Plotting the values of $\beta_{hkl}\cos\theta$ as a function of $4\sin\theta/E_{hkl}$, we determine the uniform deformation.

Stress can be calculated from the slope of the line and from lattice strain. UDSM for ZnO nanoparticles is shown in the inset of Fig. 4. In Eq. (15), we have considered the homogeneous isotropic nature of the crystal. However in many cases, the assumption of homogeneity and isotropy is not fulfilled. Moreover, all the constants of proportionality associated with the stress–strain relation are no longer independent when the strain energy density u is considered. According to Hooke's law, the energy
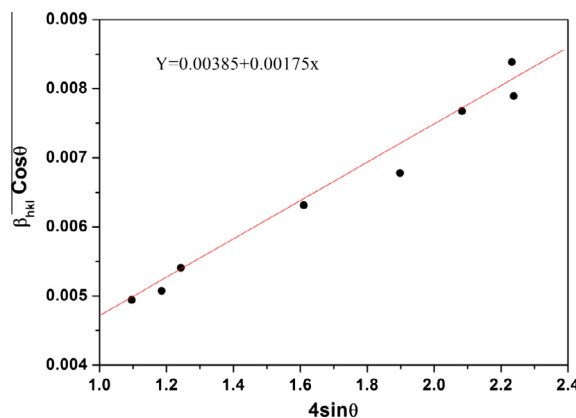
Fig. 3. Plots of $\beta_{hkl}\cos\theta$ vs $4\sin\theta$ of ZnO sample.

Table 4
Geometric parameters of the ZnO nanoparticle.

Scherrer's method D (nm)	W–H method								
	UDM		USDM			UDEDM			
	D (nm)	$\varepsilon \times 10^{-3}$	D (nm)	σ (MPa)	$\varepsilon \times 10^{-3}$	D (nm)	u (kJ m^{-3})	σ (MPa)	$\varepsilon \times 10^{-3}$
23	36.02	1.75	33.36	236.6	1.8	28	197	278.5	2.25
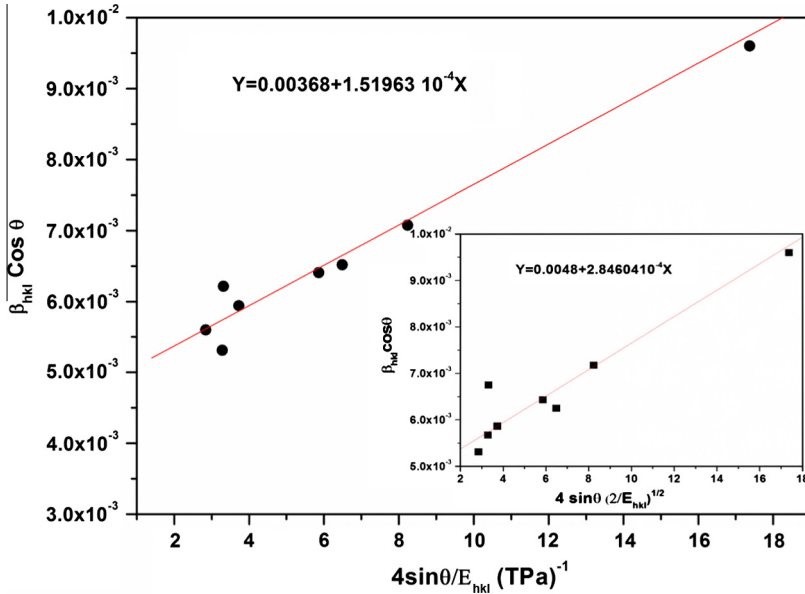
Fig. 4. Plots of $\beta_{hkl}\cos\theta$ vs $4\sin\theta/E_{hkl}$. In the inset: plots of $\beta_{hkl}\cos\theta$ vs $4\sin\theta(2/E_{hkl})^{1/2}$ of ZnO sample.

density u (energy per unit volume) as a function of strain is given by $u = \varepsilon^2 \cdot E_{hkl}/2$. Therefore, Eq. (16) can be modified to the following form Eq. (18).

The uniform deformation energy density (UDEDM) can be calculated from the slope of the line plotted between $\beta_{hkl}\cos\theta$ and $4\sin\theta(2/E_{hkl})^{1/2}$. The lattice strain can be calculated by knowing the E_{hkl} values of the sample.

The uniform deformation energy density in UDEDM was obtained from the plot drawn between $\beta_{hkl}\cos\theta$ and $4\sin\theta(2/E_{hkl})^{1/2}$, inset of Fig. 4. The value of u was calculated from the slope and the crystallite size is estimated from the y-intercept of linear fit. The results obtained from the Scherrer method and W–H models (UDM, USDM and UDEDM) are summarized in Table 4. The value of strain is lower than the values obtained for ZnO powder that have been made by other techniques. Although both USDM and UDEDM consider the anisotropic nature of the crystallites, which is not similar to UDM approach, there is no considerable difference in strain values, Table 4. Moreover, it can be clearly seen that considering the uniformity of deformation energy density in (Eq. (18)) did not affect the values for lattice strain, stress and crystallite size. The value of crystallite size D calculated by Scherrer method is less than that obtained by Williamson–Hall method. This difference is attributed to the strain value. Thus, using the Scherrer method without considering the strain may yield to inaccurate results.

3.2. DSC

Differential scanning colorimetry (DSC) of ZnO powder was carried out. ZnO powder was heated from room temperature to 413 °C. Fig. 5 shows the plot of DSC analysis. From the DSC curve, four endothermic and three exothermic peaks are found at 81 °C, 152 °C, 210 °C, 245 °C, 136 °C, 187 °C and 295 °C, respectively. These peaks are attributed to the evaporation of water and the decomposition of the hydroxide groups. In general, metal oxides such as ZnO have high melting temperature (1975 °C), and therefore, cannot be decomposed at low temperature. It is well known that ZnO sublimes at temperatures over 1200 °C under atmospheric pressure [38]. No structural change was found in ZnO up to 500 °C [39]. Thus, no extrinsic defect can be obtained at low temperature. At low temperature, ZnO demonstrates the intrinsic defect. The minimum temperature at which first defect was
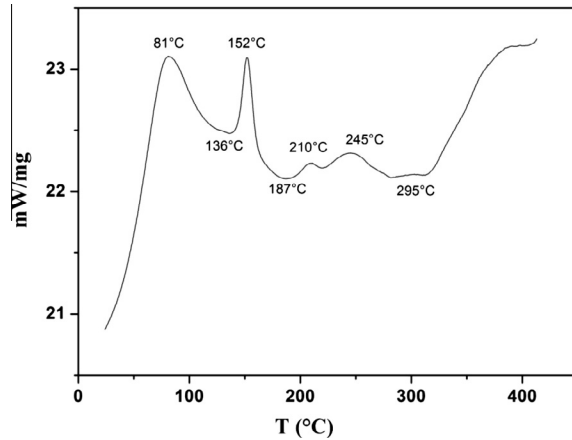
Fig. 5. DSC curve of ZnO nanoparticle.

detected is 81 °C which is obviously lower than 300 °C. And also there are three exothermic peaks below 300 °C which indicates the intrinsic defect presence in ZnO nanoparticle. The endothermic peaks were associated with disappearance of OH groups. In fact, FTIR analysis was made in order to confirm the OH behavior. Fig. 6 shows the FTIR of as-prepared ZnO powder and ZnO annealed at 200 °C. The absorption peak which is centered at 3435 cm^{-1} corresponds to the hydroxyl group OH. Also, we remark the disappearance of the hydroxyl group with annealing temperature. As show in Fig. 6, the intensity of OH bond decrease with the annealing temperature.

3.3. Micro-deformation analysis

The element compositions of ZnO powder were analyzed by energy dispersive X-ray analysis (EDX) as shown in the inset in Fig. 7. The presence of the constituent elements for ZnO, Zn and O were confirmed by the occurrence of their respective peaks. No other peaks of impurity are shown. The SEM–EDS analysis clearly shows that the sample prepared by this method has pure ZnO phases. The percentage of the element compositions are shown in the inset Table as seen in the inset in Fig. 7.
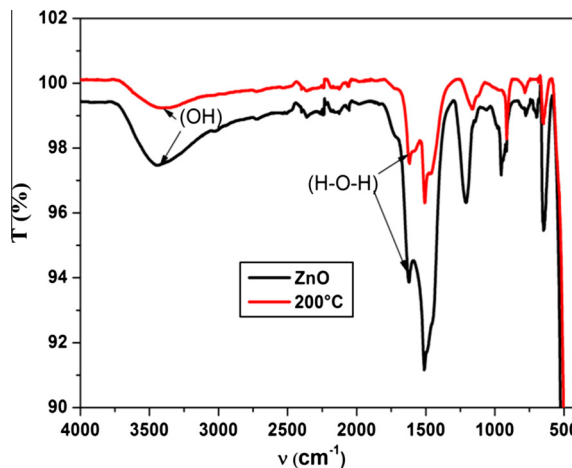
Fig. 6. FT-IR spectra of as-prepared ZnO powder and ZnO annealed at 200 °C.

Elements	Weight%	Atomie%
O K	20.39	51.14
Zn L	79.61	48.86
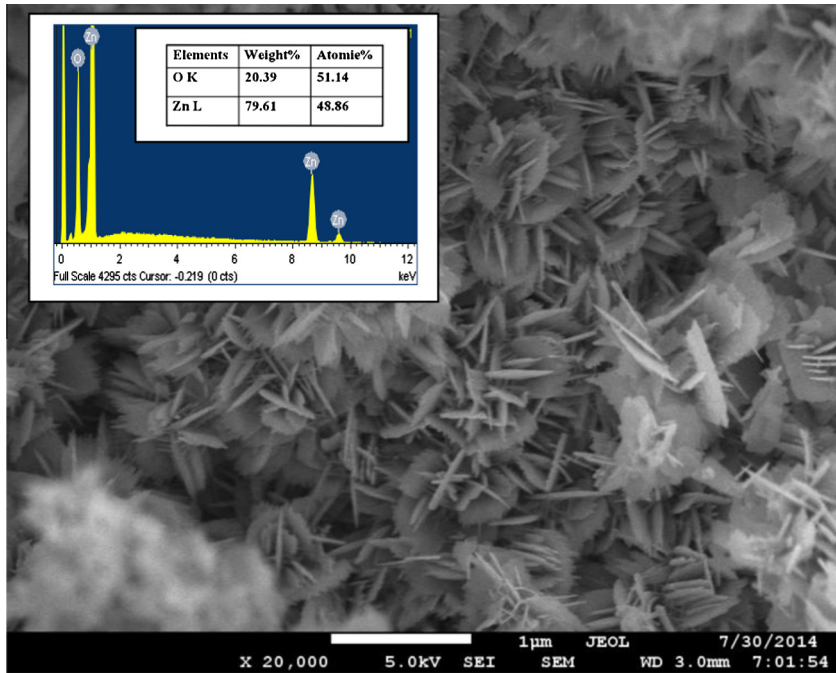
Fig. 7. SEM picture of ZnO nanoparticles. The inset: EDX spectrum and the element composition of ZnO powder.

3.4. Morphologic properties

The SEM image of ZnO sample is shown in Fig. 7. ZnO powder was formed by two-dimensional sheet with a nanometric thickness and a random distribution. The agglomeration of particles is shown in Fig. 7.

3.5. Optical properties

3.5.1. Optical energy gap

The optical properties of the as-obtained ZnO nanoparticles were studied by UV–visible spectroscopy. The absorption spectra of ZnO nanoparticle is shown in Fig. 8. A broad band is observed for the wavelength of about 369 nm in the absorption spectra which is characteristic of a pure ZnO. No other peaks were observed in the spectrum which confirms that we have synthesized a pure ZnO powder. The sharp absorption edge (369 nm), is very close to the intrinsic band gap of ZnO (3.36 eV).

The optical band gap E_g, can be estimated by the Tauc model, Eq. (19) [40].

ZnO has a direct band gap for that $n = 1/2$. The optical energy gap E_g can be obtained from the intercept of $(\alpha h\nu)^2$ vs $h\nu$ [41], in the inset in Fig. 10. The obtained values of E_g is 3.34 eV, which is in good agreement with the literature.

3.5.2. Refractive index and extinction coefficient

Refractive index is one of the fundamental properties for an optical material. The evolution of the refractive index of optical materials is considerably important for many applications. This evolution obeys to the Cauchy distribution [42] described by the relation given in Eq. (20).

In addition to the Cauchy extrapolation described above, which was done to provide reasonable values for refractive index in the spectral range of low absorption.
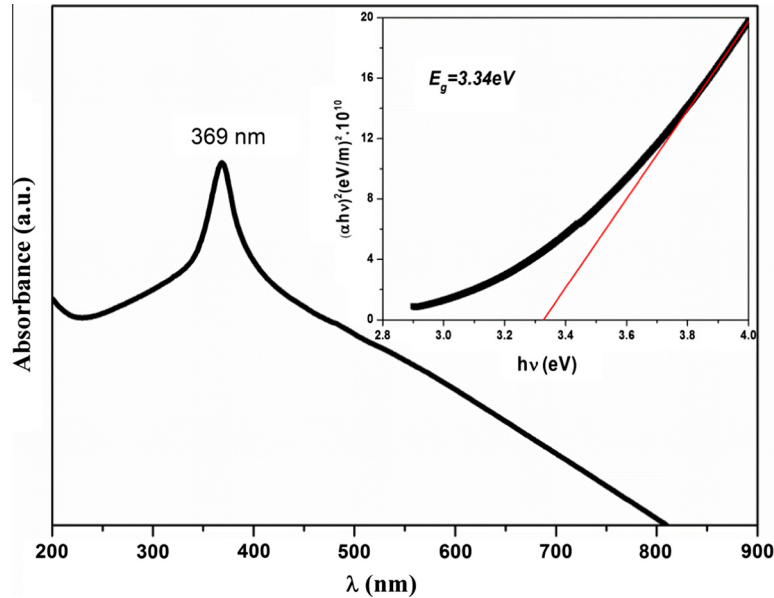
Fig. 8. Absorbance spectra of ZnO powder. In the inset: $(\alpha h\nu)^2$ vs $h\nu$ and extrapolating for optical energy gap E_g for ZnO powder.

As shown in Fig. 9, the refractive index n of ZnO powder obeys to the Cauchy law described by Eq. (20). The values of n_0, A and B are gathered in Table 5.

The evolution of refractive index with the wavelength can be also described by the model of Wemple–DiDomenico. In fact, Wemple–DiDomenico [43,44] uses a single-oscillator description of the frequency dependent dielectric constant to define a dispersion energy parameters E_d and E_0. The refractive index dispersion of the sample studied can be fitted by the Wemple–DiDomenico model. The dispersion plays an important role in the research for optical materials because it is a significant factor in optical communication and in designing devices for spectral dispersion. Although these rules are quite different in detail, one common feature is the over-whelming evidence that both crystal structure and ionicity influence the refractive index behavior of solids in ways that can be
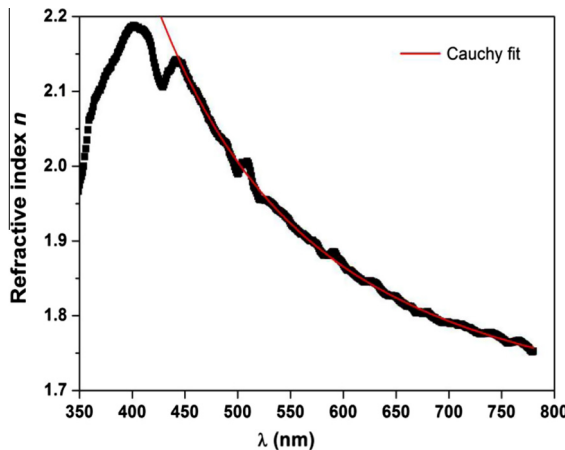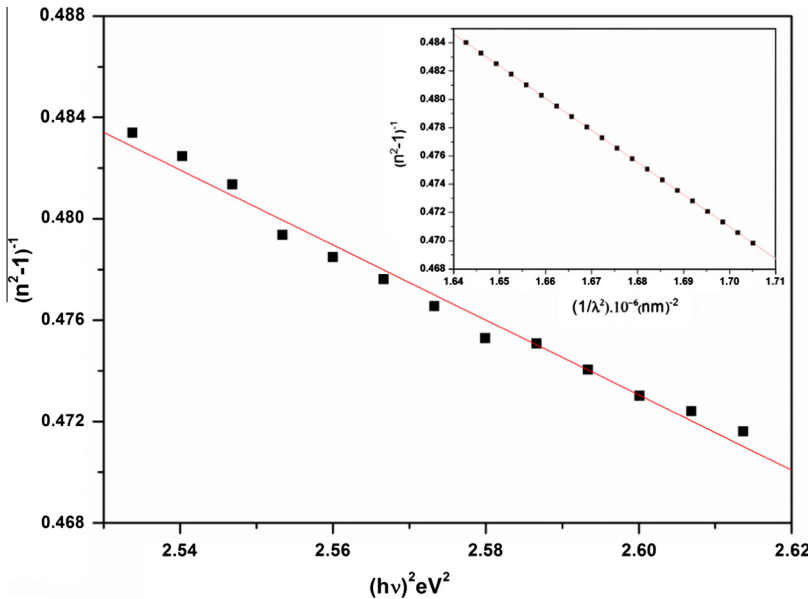

Fig. 9. Plot of the refractive index vs wavelength.

Table 5
Calculated values of parameters n_0, A, B, E_d, E_0, λ_0 and S_0.

Parameter	n_0	A (μm^{-2})	B (μm^{-4})	E_0 (eV)	E_d (eV)	λ_0 (μm)	S_0 (μm^{-2})
ZnO	1.64	0.54	0.104	2.40	2.80	0.243	28.7

Fig. 10. Plots of $(n^2 - 1)^{-1}$ vs $(h\nu)^2$. In the inset: $(n^2 - 1)^{-1}$ vs $1/\lambda^2$.

simply described [44]. The relation between the refractive index n and the single oscillator strength below the band gap is given by Eq. (21) [44,45].

The oscillator energy E_0 is an average of the optical band gap E_g^{opt}, it can be obtained from the Wemple DiDomenico model. Experimental verification of Eq. (21) can be obtained by plotting $(n^2 - 1)^{-1}$ vs $(h\nu)^2$ as illustrated in Fig. 10. E_0 and E_d values were calculated from the slope $(1/E_0 E_d)$ and intercept on the vertical axis is E_0/E_d. The values of E_0 and E_d are given in Table 5.

Under the same model, the refractive index can also be analyzed to determine the long wavelength refractive index n_∞, the average oscillator wavelength λ_0 and the oscillator length strength S_0. These values can be obtained by using the following relations respectively Eq. (22), Eq. (23) and Eq. (24).

By fitting the plots of $(n^2 - 1)^{-1}$ vs $\frac{1}{\lambda^2}$, the inset in Fig. 10, we can deduce the values of λ_0 and S_0 which are gathered in Table 5.

The extinction coefficient k was calculated from the absorption coefficient using the equation Eq. (25).

The extinction coefficient reduces to zero which means that ZnO powder has a low absorption in this range, Fig. 11.

3.5.3. Optical dielectric constant

The complex dielectric constant is a fundamental intrinsic property of the material. The real part of the dielectric constant shows how much it will slow down the speed of light in the material, whereas the imaginary part shows how much a dielectric material absorbs energy from an electric field due to the dipole motion. The knowledge of the real and imaginary parts of the dielectric constant provides information about the loss factor which is the ratio of the imaginary part to the real part of the dielectric constant. The complex dielectric constant $\varepsilon(\omega) = \varepsilon_1(\omega) - i\varepsilon_2(\omega)$ characterizes the optical properties

of the solid material. The real and imaginary parts of dielectric constant for pure ZnO are also determined by the relations given in Eq. (26) [46].

In the infrared range, ε_1 is linear function of λ^2 as seen in Fig. 12. While ε_2 is linear with λ^3 as seen in Fig. 12. These results can be used to determine the optical constants such as ε_∞, ω_P and τ which represent the dielectric constant at high frequencies, the pulse plasma and the relaxation time respectively. These parameters can be determined from the equations Eq. (27) [47,48].

We deduce the value of the optical conductivity σ_{dC} from the equation Eq. (28) [49].

The values of ε_∞, ω_p, τ, σ_{dC} and N/m^* are gathered in Table 6.

3.6. Raman scattering measurements

The structural analysis of ZnO powders was studied by X-ray diffraction and in this paragraph was further investigated by Raman spectroscopy, in experimental conditions presented in the previous
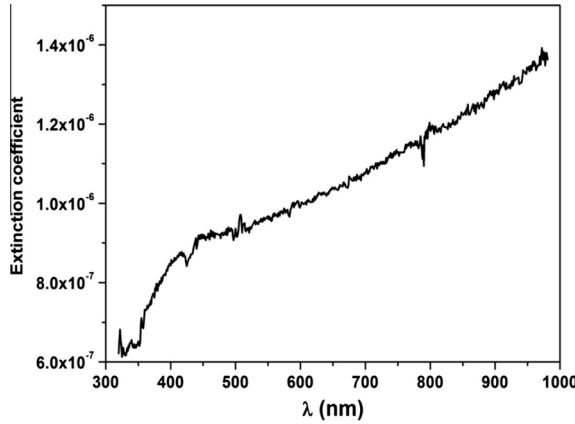

**Fig. 11.** The extinction coefficient k as a function of wavelength.
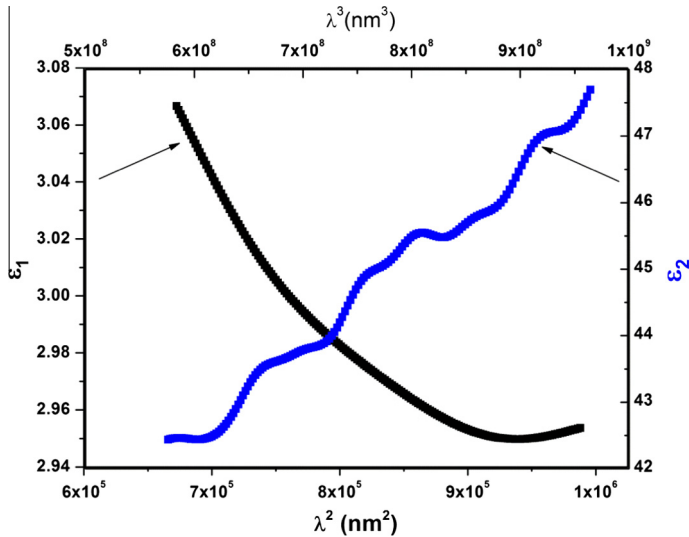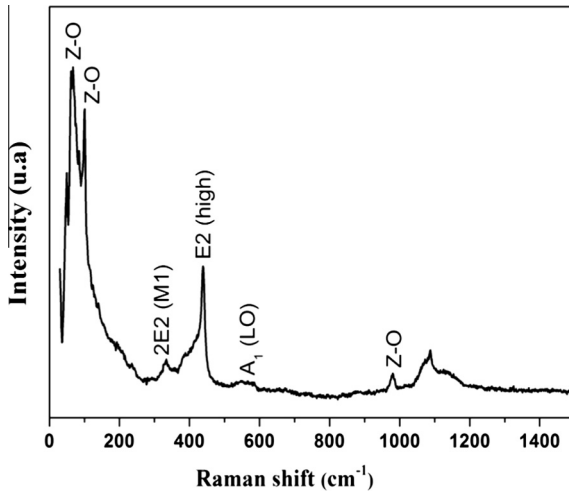
Fig. 12. ε_1 vs λ^2 and ε_2 vs λ^3.

Table 6
Calculated values of ε_∞, ω_P and other constants.

	ε_∞	ω_P (10^{14} rad s^{-1})	τ (10^{-15} s)	N/m^* (10^{47} g^{-1} cm^{-1})	σ_{dC} (S cm^{-1})
ZnO	4.31	5.70	1.4	12.53	4490.75

Fig. 13. Raman spectrum of ZnO nanoparticles.

section. Raman scattering measurements are very sensitive to the main structure, as well as the concentration and the intrinsic and extrinsic nature of defects in the crystal [49]. Thus, Raman scattering is well adapted to obtain information about the quality of the sample. ZnO has a wurtzite crystal structure with the space group C_{6v}^4($P6_3mc$) which is in accord with the literature [50]. These structures two units correspond to the formula in the original cell with all atoms occupy C_{3v} sites. The vibration modes of normal network to the Γ point of the Brillouin zone C are generally predicted by the equation of optic group theory $\Gamma = A_1 + 2E_2 + E_1 + 2B_1$ [51]. A_1 and E_1 modes are polar modes and exposure two different frequencies of the transverse optical (TO) and longitudinal optical (LO) phonon modes. Both A_1 and E_1 are infrared and Raman fashion active. E_2 mode has two frequencies E_2^{High} and E_2^{Low} is non-polar and Raman active only. B_1 mode is silent mode. E_2, A_1 (TO) and E_1 (TO) modes are identified when the incident radiation is perpendicular to the c-axis of the sample. Whereas E_2 and A_1 (LO) can be observed at the incident light parallel to the c-axis [51]. Fig. 13 shows the Raman spectra of ZnO nanoparticles recorded at room temperature. Several peaks at 68, 100, 331, 438, and 564 cm^{-1} are attributed to optical phonons of ZnO are observed. The intense and fairly narrow peak at 438 cm^{-1} corresponds to a nonpolar optical phonon E_2 (high) of wurtzite ZnO while the 331 cm^{-1} is assigned to the second-order Raman spectrum arising from zone boundary phonons of the hexagonal ZnO [52]. The low intensity Raman pics in the region 980–1100 cm^{-1} are attributed to the optical overtones and associated with the second-order Raman active modes [53]. The peak observed at 564 cm^{-1} is attributed to the A_1 (LO) mode of the hexagonal ZnO.

4. Conclusion

ZnO nanoparticles with hexagonal structure have been synthesized by direct precipitation method at room temperature. The prepared powder was characterized by XRD, DSC, SEM, EDX, UV–Visible and Raman spectroscopy. XRD and EDX show the high quality of the synthesized ZnO powder which is

proved by the presence of pure ZnO hexagonal structure phase related pics. SEM images show that the ZnO powder was formed by two-dimensional sheets with a nanometric thickness and a random distribution. The measured optical band gap for ZnO is 3.34 eV is in good agreement with literature. Raman studies indicate first and second order active modes of the ZnO. The optical characterization shows that the powder exhibits a low absorbance in the visible range. This makes the powder suitable for use as an antireflection coating for hetero-junction solar cells and optoelectronic applications.

Appendix A.

The Bragg equation leads to calculate the interplanar spacing d_{hkl}.

$$2d_{hkl} \sin \theta = n\lambda \tag{1}$$

where d_{hkl} is the interplanar spacing, θ is the Bragg angle, n is the order of diffraction, and λ is the wavelength of X-ray ($\lambda = 1.541$ Å).

For hexagonal structure the lattice parameters a and c are given by:

$$\frac{1}{d_{hkl}^2} = \frac{4}{3}\left[\frac{h^2 + hk + k^2}{a^2}\right] + \frac{l^2}{c^2} \tag{2}$$

The lattice parameters a and c were calculated from the $(1\,0\,0)$ and $(0\,0\,2)$ by using:

$$c = \frac{\lambda}{\sin \theta_{(002)}} \tag{3}$$

$$a = \frac{\lambda}{\sqrt{3} \sin \theta_{(100)}} \tag{4}$$

For hexagonal system the volume V of the unit cell was determined by using:

$$V = 0.866 \times a^2 \times c \tag{5}$$

The texture coefficient TC $(h\,k\,l)$ was calculated by:

$$TC(h\,k\,l) = \frac{I(h\,k\,l)/I_0(h\,k\,l)}{1/N\sum_0^N I(h\,k\,l)/I_0(h\,k\,l)} \tag{6}$$

The stacking fault probability α was calculated using:

$$\alpha = \left(2\pi^2/45\sqrt{3}\right)\Delta(2\theta)/\tan\theta \tag{7}$$

where θ is the position of $(h\,k\,l)$ planes and $\Delta(2\theta)$ is the peak shift for the oriented $(h\,k\,l)$ planes was measured.

The residual stress σ was calculated from the following equation:

$$\sigma = \frac{2c_{13}^2 - c_{33}(c_{11} + c_{12})}{2c_{13}} \cdot \frac{c - c_0}{c_0} \tag{8}$$

where the elastic constants C_{ij} of single-crystalline ZnO are $C_{13} = 105.1$ GPa, $C_{33} = 210.9$ GPa, $C_{11} = 209.7$ GPa, $C_{12} = 121.1$ GPa [28], and $C_0 = 5.206$ Å [24].

The grain size D can be calculated from the Debye Scherrer equation:

$$D = \frac{K\lambda}{\beta_{hkl}\cos\theta} \tag{9}$$

where β is the FWHM, θ is the Bragg's angle of different peaks and λ is the X-ray wavelength.

The dislocation density δ was calculated from the following equation:

$$\delta = \frac{1}{D^2} \tag{10}$$

The instrumental broadening (β_{hkl}) was corrected, corresponding to each diffraction peak of ZnO nanopowder using:

$$\beta_{hkl} = \lfloor (\beta_{hkl})^2_{\text{Measured}} - (\beta_{hkl})^2_{\text{Instrumental}} \rfloor \tag{11}$$

The grain size D can be estimated by:

$$D = \frac{K\lambda}{\beta_{hkl}\cos\theta} \Rightarrow \cos\theta = \frac{k\lambda}{D}\left(\frac{1}{\beta_{hkl}}\right) \tag{12}$$

where D is the grain size, k is the shape factor (0.9), λ is the wavelength of Cu Kα radiation and β_{hkl} is the peak width at half maximum intensity.

The strain ε was obtained using the following relation:

$$\varepsilon = \frac{\beta_{hkl}}{4\tan\theta} \tag{13}$$

where ε is the weighted average strain, β_{hkl} is the peak width at half maximum intensity and θ is the Bragg's angle of different peaks.

Using Williamson–Hall method which takes account of the grain size to the strain, we can deduce the grain size D and the strain ε using the following equations:

$$\beta_{hkl} = \frac{K\lambda}{D\cos\theta} + 4\varepsilon\tan\theta \tag{14}$$

$$\beta_{hkl}\cos\theta = \frac{K\lambda}{D} + 4\varepsilon\sin\theta \tag{15}$$

$$\beta_{hkl}\cos\theta = \frac{K\lambda}{D} + 4\sigma\sin\theta/E_{hkl} \tag{16}$$

Young's modulus E_{hkl} for hexagonal structure was calculated by using their elastic compliances as show in the following equation:

$$E_{hkl} = \frac{\left[h^2 + (h+2K)^2/3 + (al/c)^2\right]^2}{S_{11}\left(h^2 + (h+2K)^2/3 + S_{33}(al/c)^4 (2S_{13} + S_{44})h^2 + (h+2K)^2/3(al/c)^2\right)} \tag{17}$$

where S_{11}, S_{13}, S_{33}, and S_{44} are the elastic compliances of ZnO, and their values are 7.858×10^{-12}, 2.206×10^{-12}, 6.940×10^{-12} and $23.57 \times 10^{-12}\ \text{m}^2\ \text{N}^{-1}$, respectively [37].

$$\beta_{hkl}\cos\theta = \frac{K\lambda}{D} + \left(4\sin\theta\left(\frac{2u}{E_{hkl}}\right)^{\frac{1}{2}}\right) \tag{18}$$

where u is the energy density.

Optical band gap energy can be calculated by using the Tauc model:

$$(\alpha h v) = A(h v - E_g)^n \tag{19}$$

where A is a constant, hv is the photon energy, α is the optical absorption coefficient, E_g is the optical band gap energy and n is a parameter associated with the type of electronic transition.

The relation between the refractive index n and the wavelengths λ was described by the Cauchy distribution given by:

$$n(\lambda) = n_0 + \frac{A}{\lambda^2} + \frac{B}{\lambda^4} \tag{20}$$

where n_0, A and B are the Cauchy's parameters and λ is the wavelength of the used light.

The evolution of refractive index with the wavelength can be also described by the model of Wemple–DiDomenico given by the following equations:

$$n^2 = 1 + \frac{E_0 E_d}{E_0^2 - E^2} \tag{21}$$

where E_d and E_0 are single oscillator constants. E_0 is the energy of the effective dispersion oscillator, E_d is the so-called dispersion energy which measure the average strength of interband optical transitions.

$$\frac{n_\infty^2 - 1}{n^2 - 1} = 1 - \left(\frac{\lambda_0}{\lambda}\right)^2 \tag{22}$$

where n_∞ is the long wavelength refractive index and λ_0 is the average oscillator wavelength.

$$n_\infty^2 = 1 + S_0\lambda_0^2 \tag{23}$$

where S_0 is the oscillator length strength.

$$n^2 - 1 = \frac{S_0\lambda_0^2}{1 - (\lambda_0/\lambda)^2} \tag{24}$$

The absorption coefficient can be calculated by using:

$$k = \frac{\alpha\lambda}{4\pi} \tag{25}$$

The real and imaginary parts of dielectric constant were determined by the relations:

$$\begin{cases} (\varepsilon(\lambda) = (n(\lambda) - ik(\lambda))^2 = \varepsilon_1(\lambda) - i\varepsilon_2(\lambda) \\ \varepsilon_1(\lambda) = n(\lambda)^2 - k(\lambda)^2 \\ \varepsilon_2(\lambda) = 2n(\lambda)k(\lambda) \end{cases} \tag{26}$$

The real and imaginary parts of dielectric constant can be given by the following equations:

$$\begin{cases} \varepsilon_1 \approx \varepsilon_\infty - \frac{\varepsilon_\infty \omega_p^2}{4\pi^2 C^2}\lambda^2 \\ \varepsilon_2 = 2nk \approx \frac{\varepsilon_\infty \omega_p^2}{8\pi^3 C^3 \tau}\lambda^3 \\ \omega_p^2 = \frac{4\pi Ne^2}{\varepsilon_\infty m_e^*} \end{cases} \tag{27}$$

where ε_∞, ω_P and τ represent the dielectric constant at high frequencies, the pulse plasma and the relaxation time. N/m^* is the free carrier concentration to effective mass ratio.

Optical conductivity σ_{dC} can be obtained by:

$$\sigma_{dC} = \frac{Ne^2\tau}{m^*} \tag{28}$$

References

[1] Z.L. Wang, Nanostructures of zinc oxide, Mater. Today 7 (2004) 26–33.
[2] C.N.R. Rao, A. Govindaraj, Nanotubes and Nanowires, The RSC Nanoscience and Nanotechnology Series, Royal Society of Chemistry, London, UK, 2005.
[3] Z. Fan, J.G. Lu, Zinc oxide nanostructures: synthesis and properties, J. Nanosci. Nanotechnol. 5 (2005) 1561–1573.
[4] D. Sharma, S. Sharma, B.S. Kaith, J. Rajput, M. Kaur, Synthesis of ZnO nanoparticles using surfactant free in-air and microwave method, Appl. Surf. Sci. 257 (2011) 9661–9672.
[5] A. Eftekhari, F. Molaei, H. Arami, Flower-like bundles of ZnO nanosheets as an intermediate between hollow nanosphere and nanoparticles, Mater. Sci. Eng. A 437 (2006) 446–450.
[6] K.D. Kim, D.W. Choi, Y.-H. Choa, H.T. Kim, Optimization of parameters for the synthesis of zinc oxide nanoparticles by Taguchi robust design method, Colloids Surf. A: Physicochem. Eng. Aspects 311 (2007) 170–173.
[7] S. Cho, S.H. Jung, K.H. Lee, Morphology-controlled growth of ZnO nanostructures using microwave irradiation: from basic to complex structures, J. Phys. Chem. C 112 (2008) 12769–12776.
[8] H. Cheng, J. Cheng, Y. Zhang, Q.-M. Wang, Large-scale fabrication of ZnO micro-and nano-structures by microwave thermal evaporation deposition, J. Cryst. Growth 299 (2007) 34–40.
[9] M.S. Takumoto, S.H. Pulcinelli, C.V. Santilli, V. Briois, J. Phys. Chem. B 107 (2003) 568.
[10] M. Singhai, V. Chhabra, P. Kang, D.O. Shah, Synthesis of nanoparticles for varistor application using Zn-substituted aerosol OT microemulsion, Mater. Res. Bull. 32 (1997) 239–247.
[11] F. Rataboul, C. Nayral, M.J. Casanove, A. Maisonnat, B. Chaudret, Synthesis and characterization of monodisperse zinc and zinc oxide nanoparticles from the organometallic precursor [Zn(C$_6$H$_{11}$)$_2$], J. Organomet. Chem. 643–644 (2002) 307–312.
[12] K. Okuyama, I.W. Lenggoro, Preparation of nanoparticles via spray route, Chem. Eng. Sci. 58 (2003) 537–547.
[13] A.B. Moghaddam, T. Nazari, J. Badraghi, M. Kazemzad, Synthesis of ZnO nanoparticles and electrodeposition of polypyrrole/ZnO nanocomposite film, Int. J. Electrochem. Sci. 4 (2009) 247–257.

[14] Y.-L. Wei, P.-C. Chang, Characteristics of nano zinc oxide synthesized under ultrasonic, J. Phys. Chem. Solids 69 (2008) 688–692.

[15] X.-L. Hu, Y.-J. Zhu, S.-W. Wang, Sonochemical and microwave-assisted synthesis of linked single-crystalline ZnO rods, Mater. Chem. Phys. 88 (2004) 421–426.

[16] J.-J. Wu, S.-C. Liu, Low-temperature growth of well-aligned ZnO nanorods by chemical vapor deposition, Adv. Mater. 14 (2002) 215–218.

[17] H.J. Zhai, W.H. Wu, F. Lu, H.-S. Wang, C. Wang, Mater. Chem. Phys. 112 (2008) 1024–1028.

[18] M. Bitenc, M. Marinsek, Z. Crnjak Orel, Preparation and characterization of zinc hydroxide carbonate and porous zinc oxide particles, J. Eur. Ceram. Soc. 28 (2008) 2915–2921.

[19] J. Zhou, F. Zhao, Y. Wang, Y. Zhang, L. Yang, Size-controlled synthesis of ZnO nanoparticles and their photoluminescence properties, J. Lumin. 122–123 (2007) 195–197.

[20] Z.M. Khoshhesab, M. Sarfaraz, M.A. Asadabad, Preparation of ZnO nanostructures by chemical precipitation method, Synth. React. Inorg., Met.-Org., Nano-Met. Chem. 41 (2011) 814–819.

[21] B.D. Cullity, S. Rstock, Elements of X-ray Diffraction, Prentice Hall, New Jersey, 2001.

[22] T.P. Rao, M.C. Santhosh kumar, A. Safarulla, V. Ganesan, S.R. Barman, C. Sanjeeviraja, Physical properties of ZnO thin films deposited at various substrate temperature using spray pyrolysis, Physica B 405 (2010) 2226.

[23] Y. Caglar, S. Aksoy, S. Ilican, M. Cagmar, Crystalline structure and morphological properties of undoped and Sn doped ZnO thin films, Superlattices Microstruct. 46 (2009) 469–475.

[24] P. Scherrer, Goettinger Nachr. 2 (1918) 98.

[25] M.K. Puchet, P.Y. Timbrell, R.N. Lamb, J. Vac. Sci. Technol. 14 (1996) 2220–2230.

[26] M.M. Abdullah, Preeti Singh, M. Hasmuddin, G. Bhagavannarayana, M.A. Wahab, In-situ growth and ab-initio optical characterizations of amorphous Ga_3Se_4 thin film: a new chalcogenide compound semiconductor thin film, Scripta Mater. 69 (2013) 381.

[27] T. Mahalingam, V.S. John, L.S. Hsu, Microstructural analysis of electrodeposited zinc oxide thin films, J. New Mater. Electrochem. Syst. 10 (2007) 9–14.

[28] T. Prasada Rao, M.C. Santhosh Kumar, A. Safarullaa, V. Ganesan, S.R. Barman, C. Sanjeeviraja, Physical properties of ZnO thin films deposited at various substrate temperatures using spray pyrolysis, Physica B 405 (2010) 2226–2231.

[29] E.L. Papadopoulou, M. Varda, K. Kouroupis-Agalou, M. Androulidaki, E. Chikoidze, P. Galtier, G. Huyberechts, E. Aperathitis, Undoped and Al-doped ZnO films with tuned properties grown by pulsed laser deposition, Thin Solid Films 516 (2008) 8141–8145.

[30] M. Ali Yıldırım, Aytunç Ates, Influence of films thickness and structure on the photo-response of ZnO films, Opt. Commun. 283 (2010) 1370–1377.

[31] L. Motevalizadeh, Z. Heidary, Facile template-free hydrothermal synthesis and microstrain measurement of ZnO nanorods, Bull. Mater. Sci. 37 (2014) 397–405.

[32] C. Suryanarayana, M. Grant Norton, X-ray Diffraction: A Practical Approach, Springer, New York, 1998.

[33] S. Adachi, Handbook on Physical Properties of Semiconductors, Springer, New York, 2004.

[34] Jian-Min Zhang, Yan Zhang, Ke-Wei Xu, Vincent Ji, General compliance transformation relation and applications for anisotropic hexagonal metals, Solid State Commun. 139 (2006) 87.

[35] D. Balzar, H. Ledbetter, Voigt-function modeling in Fourier analysis of size- and strain-broadened X-ray diffraction peaks, J. Appl. Crystallogr. 26 (1993) 97.

[36] B.E. Warren, B.L. Averbach, The effect of cold-work distortion on X-ray patterns, J. Appl. Phys. 21 (1950) 595.

[37] J.F. Nye, Physical Properties of Crystals: Their Representation by Tensors and Matrices, (Anglais), Broché, Oxford Science Publications, 1985.

[38] M.M. Abdullah, Mohammed M. Rahman, Houcine Bouzid, M. Faisal, Sher Bahadar Khan, S.A. Al-Sayari1, Adel A. Ismail, J. Rare Earths 33 (2015) 214.

[39] Dale Eric Wurster, Euichaul Oh, Jonas C.T. Wang, Determination of the mechanism for the decrease in zinc oxide surface area upon high-temperature drying, J. Pharm. Sci. 84 (1995) 1301.

[40] H. Nagabhushana, B.M. Nagabhushana, M. Kumar, H.B. Premkumar, C. Shivakumara, R.P.S. Chakradhar, Synthesis, characterization and photoluminescence properties of $CaSiO_3:Dy^{3+}$ nanophosphors, Philos. Magn. 90 (2010) 3567–3579.

[41] J. Tauc, R. Grigorovichi, A. Vancu, Optical properties and electronic structure of amorphous germanium, Phys. Status Solidi 15 (1966) 627.

[42] H.G. Tompkins, W.A. McGahan, Spectroscopic Ellipsometry and Reflectometry, John Wiley & Sons Inc., New York, 1999.

[43] S.H. Wemple, M. Didomenico, Oxygen-octahedra ferroelectrics. I. Theory of electro-optical and nonlinear optical effects, J. Appl. Phys. 40 (1969) 720.

[44] S.H. Wemple, M. Didomenico, Phys. Rev. B 3 (1971) 1338.

[45] M.A. Omar, Elementary Solid State Physics, Addison-Wesley Publishing Company, New York, 1993.

[46] M. Sesha Reddy, K.T. Ramakrishna Reddy, B.S. Naidu, P.J. Reddy, Optical constants of polycrystalline $CuGaTe_2$ films, Opt. Mater. 4 (1995) 787–790.

[47] A. Amlouk, K. Boubaker, M. Amlouk, J. Alloys Compd. 490 (2010) 602–604.

[48] F. Gervais, Optical conductivity of oxides, Mater. Sci. Eng. R 39 (2002) 29–92.

[49] C.A. Arguello, D.L. Rousseau, S.P.S. Porto, First-order Raman effect in wurtzite-type crystals, Phys. Rev. 181 (1969) 1351–1363.

[50] D. Shuang, J.B. Wang, X.L. Zhong, H.L. Yan, Raman scattering and cathodoluminescence properties of flower-like manganese doped ZnO nanorods, Mater. Sci. Semicond. Process. 10 (2007) 97–102.

[51] F. Decremps, J. Pellicer-Porres, A.M. Saitta, J.C. Chervin, A. Polian, High-pressure Raman spectroscopy study of wurtzite ZnO, Phys. Rev. B 65 (2002) 092101.

[52] K.A. Alim, V.A. Fonoberov, M. Shamsa, A.A. Balandin, Micro-Raman investigation of optical phonons in ZnO nanocrystals, J. Appl. Phys. 97 (2005) 124313–124323.

[53] G.J. Exarhos, S.K. Sharma, Influence of processing variables on the structure and properties of ZnO films, Thin Solid Films 270 (1995) 27–32.